

Wake Generated Downstream of a Vertical Axis Tidal Turbine

Pablo Ouro, Thorsten Stoesser

Hydro-environmental Research Centre, Cardiff University, CF24 3AA, Cardiff, U.K.

E-mail: OuroBarbaP@cardiff.ac.uk

Abstract—Characterising the physics involved in the wake developed downstream of vertical axis tidal stream turbines (VATTs) is a cornerstone towards understanding turbine-to-turbine interactions and thus optimise their deployment in arrays. The flow field developed around these devices is not exempt of complexity accentuated by complex blade-vortex interactions occurring within the blades swept perimeter. This publication analyses the flow characteristics of the near-wake behind a three-bladed VATT rotating at different rotational speeds using a highly accurate computational approach. Results of mean velocities and turbulent kinetic energy are validated with experiments and compared to other RANS-based numerical results. A great match with the experimental data is achieved outlining the suitability of the proposed numerical approach to represent the complex flow around VATTs. Results evidence that at low tip speed ratios the flow passes through the turbine rotor without major obstruction of the blades. Meanwhile, at higher speeds there is a minimum incident flow entraining within the rotor swept perimeter which induces the generation of the Magnus effect. The outcomes encourage to extend the applicability of the presented method to the future design of VATT arrays enhancing inter-turbine interaction and thus maximising power generation.

Index Terms—Tidal Stream turbine, Vertical Axis Tidal Turbine, Large-Eddy Simulation, Blade-vortex interaction, Tidal Energy

I. INTRODUCTION

Tidal energy is gaining momentum thanks to the successful accomplishments obtained in several tidal energy projects, mainly located along the shorelines of Canada, France or UK. These advancements are key for this promising renewable energy resource to become an economically viable alternative which can cover up to 15% of Europe's electricity demand by 2050 [1]. Tides are in continuous movement, and hence these can be predicted, making tidal energy an excellent carbon-free resource to partner with wind and solar energies as it could overcome some of the drawbacks from the latter resources, e.g. generating electricity during the night and dependency on weather conditions. Most tidal energy projects consider the deployment of tidal stream turbines which extract the kinetic energy from high speed currents and are often deployed in arrays.

At present, Horizontal Axis Tidal Turbines (HATTs) are the main beneficiaries of such favourable situation as they have achieved an advanced technological development thanks to the large investment dedicated to their investigation in the last decade [2]. HATTs provide high energy conversion rates which maximise energy extraction from tidal streams. Nonetheless, they rely on yaw mechanisms to adapt the rotor

orientation to that of the tide. On the other hand, Vertical Axis Tidal Turbines (VATTs) present many advantages that are very attractive to tidal driven flows such as omni-directionality, i.e. independence of flow direction, or lower operational tip speed ratio range which reduces noise generation and fish mortality. Despite these advantages, their lower performance compared to that of HATTs has notably reduced their consideration in tidal energy projects.

Understanding both near- and far-wake developed downstream of tidal stream turbines is vital for their deployment in arrays. These devices trigger turbulence intensity levels in their wake even at many diameters downstream which can negatively affect the turbines downstream [3]. To date no study has focused on the experimental array deployment of VATTs although this has been already accomplished in the deployment of Vertical Axis Wind Turbines (VAWTs). Kinzel et al. [4] studied the aerodynamics developed in an array of VAWTs grouped in a confined region, and outlined that inter-turbine interaction can enhance velocity deficit recovery. They showed that, if adequately arranged, the array of VAWT can provide similar, or even larger, power density (i.e. generated power per planform area) than that from analogous HAWT configurations. The fact VATTs can achieve faster velocity deficit recovery than HATTs may be related to the lack of axial swirl motion induced into the wake. The latter is the major-player in the far-wake developed behind HATTs which is the responsible of the meandering motion of wake [5], [6].

Experimental tests undertaken to study the wake dynamics of a single VATT are limited due to the technical difficulty to be performed and the high economic costs of running the tests in the required large facilities. Tescione et al. [7] studied the near-wake behind a VAWT identifying a large presence of tip vortices and how these interact with the blades during their upstroke and downstroke motions. Bachant et al. [8] measured the wake at one diameter downstream a VATT and remarked the notable asymmetry in the wake, while Araya et al. [9] showed that the wake characteristics depend on the number of blades comprising the rotor and their rotational speed.

Numerical approaches arise as a faster and cheaper alternative that can help to provide the full picture of the mechanisms involved in the wake dynamics although they have to be accurate enough to provide trustworthy data. For instance, Bachant et al. [8] employed an actuator disk model embedded into a RANS solver to reproduce the wake dynamics of a single VATT, which failed to provide accurate predictions of

the near-wake. Shamsoddin et al. [10] employed Large-Eddy Simulation (LES) to resolve the fluid flow and an actuator line method to represent the turbine's geometry, which provided good results for mean velocities whereas it underestimated Reynolds stresses values. Both actuator disk and actuator line approaches do not represent the physical blade geometry and hence lack of resolving dynamic stall at the blades [8]. This limitation makes these models to be commonly employed in the prediction of the far-wake dynamics instead of the near-wake.

Geometry resolved approaches are needed for achieving a correct resolution of the flow field developed at the blades, e.g. dynamic stall. Ouro et al. [11] adopted an immersed boundary method to represent the turbine blades embedded into a LES solver. They revealed the complex fluid-structure interaction mechanisms developed in the blades along their rotation cycle, which changed notably depending on the rotational speeds. At low speeds, the blades undergo deep dynamic stall, i.e. experience full flow separation along most of the revolution, whereas at high rotational speeds light dynamic stall is present. The visualisations from [11] provided sufficient evidence that the resulting Blade-Vortex Interaction (BVI) mechanisms in the inner-wake are responsible for the changes in performance and operational tip speed ratio range of VATTs, which vary depending on the blade shape comprising the rotor and its solidity.

The near-wake properties result from the BVIs happening into the inner-wake. VATT blades generate a different flow field during the two halves of their revolution causing the near-wake to be asymmetry in the horizontal plane [8], [12]. Tescione et al. [7] highlighted that VATTs wake is also asymmetry in the vertical direction and that the near-wake skewness is attributed to the rotational motion of the turbine. These properties are intrinsic of VATTs as the blades travel in the same and opposite directions to the incident flow during their upstream and downstream motion, and hence generate an uneven loading-cycle and velocity distribution in the wake [11]. The degree of asymmetry depends on both solidity (i.e. geometry of the turbine) and rotational speed, among other factor such as the free-stream velocity. Araya et al. [9] defined the dynamic solidity as a parameter that indicates how the VATT's wake compares to that of a bluff-body, such as rotating cylinder [13].

The current publication analyses the near-wake developed downstream a single VATT operating at different rotational speeds. The device is simulated using a highly accurate numerical approach based on the coupling of an Immersed Boundary method into a Large-Eddy Simulation (LES-IB) solver which was already validated to predict the performance of VATTs [11]. Results of the velocity field are validated with the experimental measurements from Mercier et al. [12], who additionally reported RANS results and are also used for further comparison with the present LES. Time-averaged velocity field and turbulent kinetic energy values are reported for different tip speed ratios in order to study the influence of the dynamic solidity in the shape of the wake.

II. NUMERICAL FRAMEWORK

The spatially filtered incompressible Navier-Stokes equations are resolved to perform LES using the in-house code Hydro3D [14], [15]. Eq. 1 and 2 are solved in a rectangular Cartesian grid using fourth-order finite differences and staggered velocity storage.

$$\frac{\partial u_i}{\partial x_i} = 0 \quad (1)$$

$$\frac{\partial u_i}{\partial t} + \frac{\partial u_i u_j}{\partial x_j} = -\frac{\partial p}{\partial x_j} + \nu \frac{\partial^2 u_i}{\partial x_i x_j} - \frac{\partial \tau_{ij}}{\partial x_j} + f_i \quad (2)$$

Here u_i and x_i (where $i, j = 1, 2, 3$) are the filtered fluid velocity and coordinates, p denotes filtered pressure, ν represents the kinematic viscosity of the fluid, τ is the subgrid stresses tensor, and f_i corresponds to the forcing term from the Immersed Boundary (IB) method.

A fractional step method [16] is used to time advance the governing equations using a three-steps low-storage Runge-Kutta to calculate convective and viscous terms [17]. These terms provide the predicted non-solenoidal fluid velocity field. A corrector step is then performed using a multigrid technique to solve the Poisson pressure equation in order to generate a pressure field onto which the predicted velocities are projected so the divergence-free condition is satisfied. Wall-Adapting Local Eddy-viscosity (WALE) subgrid scale (sgs) model [18] is adopted to account for the subgrid stresses as it does not require the explicit calculation of the sgs-viscosity near the walls, which suits well with the use of moving immersed boundaries [11].

The direct forcing IB method from [19] is adopted to simulate the moving solid geometries. The turbine blades are discretised into a set of individual Lagrangian markers which represent the desired hydrofoil geometry [11]. The total set of discrete Lagrangian markers conforms the solid grid and this is physically decoupled from the fluid mesh which allows the latter to be continuous along the computational domain, i.e. not conformed to the solid, and thus to use fast flow solvers, e.g. multigrid techniques. The fluid and solid frameworks are communicated through a three-steps procedure. First, the fluid velocities, u_i , are transferred to the solid grid to obtain the interpolated Lagrangian velocities, U_L , through Eq. 3 where Δx_i represents the fluid grid cell area and n_e is the number of Eulerian neighbours considered.

$$U_L = \sum_{i=1}^{n_e} u_i \cdot \delta(x_i - X_L) \cdot \Delta x_i \quad (3)$$

The solid force F_L is calculated in Eq. 4 as a result of the difference between the desired or forced velocity (U_L^*) of the solid and the actual fluid velocity (U_L).

$$F_L = \frac{U_L^* - U_L}{\Delta t} \quad (4)$$

Finally, the fluid is corrected with the forcing term f_i to

enforce the solid velocity in the fluid mesh, as

$$f_i = \sum_{L=1}^{n_L} F_L \cdot \delta(X_L - x_i) \cdot \Delta V_L \quad (5)$$

Note that the backwards interpolation (Eq. 5) considers n_L Lagrangian neighbours which have an assigned volume of ΔV_L which is approximately equal to Δx_i . This is required to guarantee the stability of the method as the interpolating delta functions (δ) with the kernel function from [20] are adopted [11].

Hydro3D features a local mesh refinement method that allows to refine certain regions of the domain and in combination with the IB method permits to perform LES of moving bodies using a feasible amount of computational resources and within a reasonable time-frame. The LES-IB method has been presented, validated and applied to analyse the performance of tidal stream turbines in [6], [11].

III. NUMERICAL SETUP

A VATT comprised of three cambered NACA 0018 is simulated and results from the LES-IB method are validated with experimental data and compared with RANS-based numerical results both reported by Mercier et al. [12]. The length of the turbine blades is the same than its diameter (D) and equal to 0.175m. The blades chord length (c) is 0.032m providing a solidity ($\sigma = N_b c / 2\pi R$, where N_b is the number of blades and R is the turbine's radius) of 0.175. The experiments were conducted at the LEGI flume which measures 1m x 0.7m x 0.25m in x -, y - and z -directions and is bounded by walls both at the sides and top and bottom. The resulting blockage factor ($\beta = D/L$, where L stands for the width of the channel) relates the transversal area of the channel with the projected area of the turbine and is equal to 0.25. The extension of the computational domain, illustrated in Fig. 1, represents the horizontal dimensions of the flume whilst the domain is limited to 0.064m ($2c$) in the spanwise direction, as the simulation of the whole flume is unaffordable regarding the computational resources available to the authors. The turbine rotation axis is located $1.5D$ away from the inlet.

At the inlet a uniform free-stream velocity, U_0 , equal to 2.3m/s is prescribed during the simulation, which corresponds to a Reynolds number based on the chord ($Re_c = U_0 c / \nu$) of 73,600. At the outlet a convective boundary condition is adopted while no-slip is imposed to the lateral sides of the domain representing the experimental flume walls. Periodic boundary conditions are set in the spanwise direction.

The turbine rotates counter-clockwise with fixed rotational speed, Ω , as in the experiments the device is motor-driven, i.e. a constant rotation is induced to the shaft. Note that Araya et al. [21] proved that the characteristics of the wake developed downstream of a VATT are very similar when the device rotates as the action of the flow (torque-driven) or a certain velocity is prescribed to the rotor (motor-driven). In order to characterise the wake produced at different rotational speeds, tip speed ratios ($\lambda = \Omega R / U_0$) of 1.5, 2.0 and 3.0 are analysed. This range of simulations would allow to analyse the wake

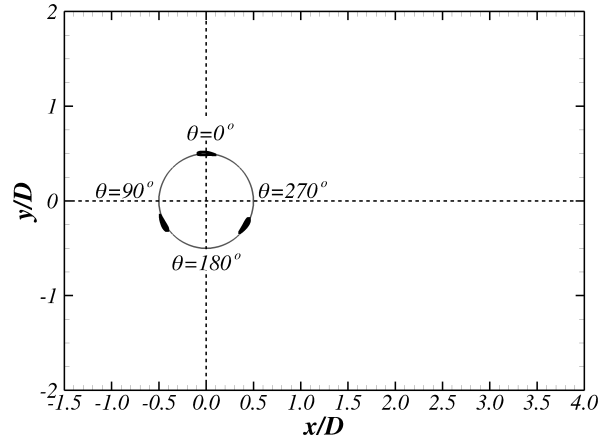


Fig. 1. Representation of the numerical domain. Flow direction goes from left to right and the turbine rotates counter-clockwise.

when the turbine operates at its optimum performance, i.e. $\lambda = 2.0$ (see Fig. 2), and compared it to that developed when it under- and over-spins, i.e. for $\lambda = 1.5$ and 3.0 respectively.

The same experimental setup from Mercier et al. [12] was also adopted by Maitre et al. [22], who focused on understanding the turbine's performance instead of the developed wake. Ouro et al. [11] used the results from [22] to validate the capabilities of the adopted LES-IB method to reproduce the power performance of the device. Fig. 2 shows the power coefficient (C_P) for different tip speed ratios obtained in the experiments [22] and with LES [11]. Results show that the LES-IB method is capable of predicting the turbine performance at all tip speed ratios mainly due to its capability of resolving the main turbulent structures that dominate the flow around the blades, such as leading and trailing edge vortices originated during deep and light dynamic stall conditions.

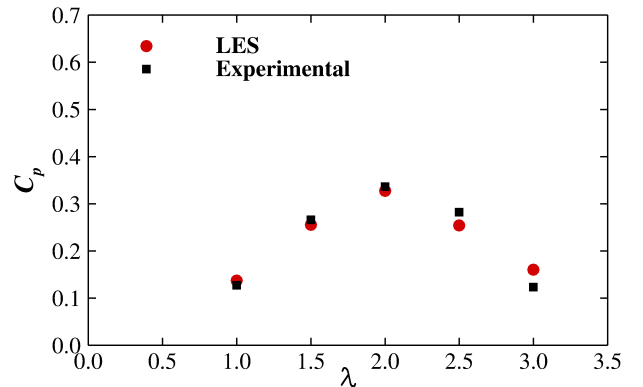


Fig. 2. Comparison of the power coefficient (C_P) for different tip speed ratios between experiments [22] and LES [11].

In the current simulations, the mesh resolution is set to $\Delta x/c = \Delta y/c = 0.01$ and $\Delta z/c = 2\Delta x/c$, and the time step is $\Delta t^* = \Delta t U_0 / c = 4 \cdot 10^{-4}$. This setup is adopted as a result of the spatial and temporal integration sensitivity study presented in [11] which proved to provide sufficient accuracy. Initially, two turbine revolutions are performed in

order to allow the flow to develop, and since this stage mean velocity statistics are computed. After 6 revolutions, turbulence statistics start to be collected until a total of 10 spins are completed. The simulations run using 171 cores in HPC Wales supercomputing facilities and have an average computational load of 24,000 CPU hours.

IV. RESULTS

A. Hydrodynamics validation

The validation of the wake developed downstream of the VATT predicted with the LES-IB method is done for the case the device rotates at tip speed ratio of 2.0, and results are compared with experimental and 2D RANS data presented in [12]. Fig. 3 and 4 show the contours of normalised streamwise velocity (U/U_0) and z-vorticity ($\omega_z c/U_0$) along a xy -plane at half spanwise domain length, i.e. $z/c = 1$. A low-momentum area is depicted from Fig. 3 as a result of the energy extraction of the turbine from the incident flow. It is also noticed that due to the turbine blockage, there are two regions of flow acceleration in between the side walls and the turbine ($|y/D| > 0.5$).

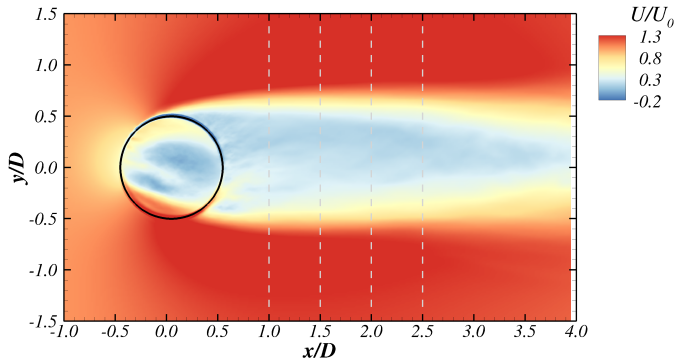


Fig. 3. Contours of normalised streamwise velocity at $z/c = 1$ for the turbine rotating at $\lambda = 2.0$.

Fig. 4 shows the low-velocity area from Fig. 3 is bounded by two streams distributed along $y/D \approx \pm(0.6-0.7)$ that feature high levels of vorticity of opposite sign, which coincides well with the experimental observations [12]. The large vorticity levels in these regions result from the instability due to the energetic vortices shed from the blades. According to [11], the negative vorticity stream (blue contour in Fig. 4) corresponds to trailing edge separation vortices shed between $300^\circ < \theta < 30^\circ$ which is the region of highest relative velocity, i.e. difference between the blades and incident flow velocities. On the contrary, dynamic stall vortices are shed along the downstream side of the revolution approximately at $\theta \approx 120^\circ$ and 230° corresponding to those angles where the effective angle of attack is maximum [11].

The wake expands laterally until $x/D \approx 1.0$, as a result of the convection of large-scale vortices, with maximum extension values of $|y/D| \approx \pm 0.85$ representing a considerable wake widening compared to the maximum value of $|y/D| = 0.5$ swept by the blades. This generated shear layer

maintains its extension fairly uniform until $x/D \approx 2.5$ from which the high-vorticity streams start to converge as also appreciated from the flow streamlines of Fig. 4.

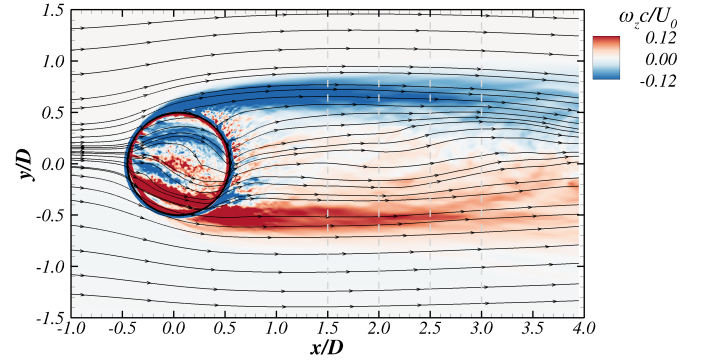


Fig. 4. Contours of normalised spanwise vorticity at $z/c = 1$ for the turbine rotating at $\lambda = 2.0$. Black circle represents the blades' swept perimeter.

A qualitative comparison of the computed wake with experiments and RANS results [12] is presented in Fig. 5 with profiles of mean normalised streamwise velocities and turbulent kinetic energy (TKE) at four transversal locations outlined with dashed lines in Fig. 3. Time-averaging of mean velocities is performed between revolutions 3 to 10 whilst second order statistics averaging is done between spins 7 to 10. Analogously to the results reported in [12], TKE is calculated from the two-dimensional velocity components as,

$$k = 0.5(u'^2 + v'^2) \quad (6)$$

where u' and v' are the time-averaged x- and y-velocity fluctuations respectively.

At the closest location to the turbine, i.e. at $x/D = 1.0$ shown in Fig. 5a), the distribution of the streamwise velocity from LES achieves a good agreement with both experimental and RANS results. In the TKE distribution at this location (Fig. 5e)), LES predicts well the location and extension of the two high TKE areas whose largest values are at $y/D \approx \pm 0.6$, although the LES predicted peak values are overestimated compared to those from the experiments. The present TKE values are obtained from averaging four revolutions while experiments and RANS data are averaged for a single revolution [12], which can lead to the mismatch in the TKE values at the profile closest to the turbine. An additional source of discrepancy is that the present model does not include the struts connecting the blades and shaft located in the horizontal plane of the experimental measurements, which might affect the convection of the vortices originated during the BVI in the inner-wake and hence developing lower TKE levels.

At $x/D = 1.5, 2.0$ and 2.5 , the velocity profiles predicted by LES match the experimental values especially at the low-momentum area, i.e. $|y/D| < 0.5$, as shown in Fig. 5b) to d). Note that the distribution of the streamwise velocity profiles smoothly evolves from a "U" shape found at $x/D = 1.0$ to a "V" shape, which is clearly observed at $x/D = 2.5$. This agrees with the velocity contours from Fig. 3 where

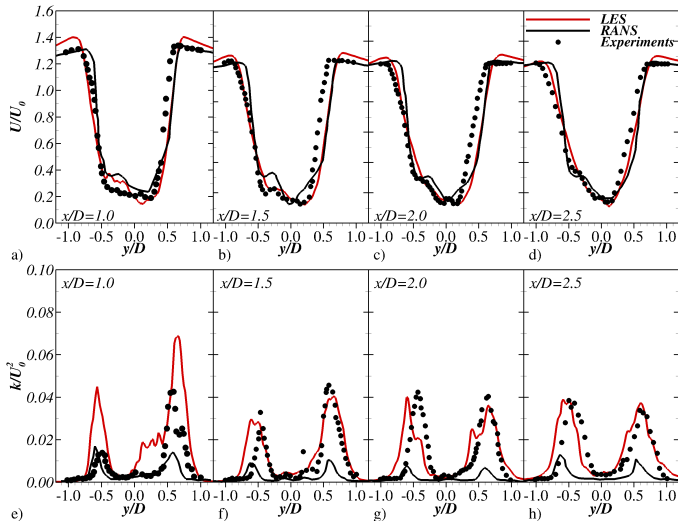


Fig. 5. Profiles of normalised mean streamwise velocity profiles and TKE at $x/D = 1.0, 1.5, 2.0,$ and 2.5 . Comparison of the present LES results with RANS and experimental data from [12].

the transversal extension of the low-velocity area shortens when increasing the distance from the turbine. The location of the lowest velocity is consistently shifted towards $y/D > 0$ corresponding to the downstream area where the blades travel upstream and hence obstruct the incident flow the most, i.e. $270^\circ < \theta < 90^\circ$ [8], [9].

Fig. 5f) to h) show the TKE profiles at $x/D = 1.5, 2.0$ and 2.5 . LES also shows an excellent match with experiments both in terms of TKE peak values and their location. These areas of high TKE coincide with the location of the high-vorticity streams from Fig. 4 representing the pathways described by the energetic vortices shed from the blades during their convection downstream. These outcomes highlight the capabilities of LES as an eddy-resolving method capable of accurately resolving the turbulent field around the turbine in contrast to the time-averaged nature of RANS, which tends to underestimate the turbulent velocity fluctuations.

B. Wake developed at $\lambda=1.5$ and 3.0

VATTs are flow-driven devices as they spin as an action of the torque generated by the incident flow. Hence, these are expected to over- and under-spin in reference to the rotational velocity at which the device performance is the best, the so-called optimum tip speed ratio. When the turbine over-spins, the fast rotation of the blades allows less incident flow to penetrate within the swept perimeter, whereas an opposite situation is found when it under-spins. Additionally, the inner-wake exhibits a different pattern when the turbine spins at different speeds, e.g. blade-vortex interaction mechanisms [11], which are also expected to affect the near-wake behind the turbine [8].

Results for $\lambda=1.5$

Fig. 6 presents mean z-vorticity contours with the turbine spinning at $\lambda = 1.5$. Some wake characteristics are shared

with those from $\lambda = 2.0$, such as the expansion of the high-vorticity streams until $x/D = 1.0$. Beyond this point and further downstream, the high-vorticity streams representing the wake shear layer keep a fairly constant separation in the transversal direction. The streamlines in the wake are almost parallel to the ones in the outskirts flow indicating the incident flow travels through the rotor experiencing a minimal disturbance from the rotational motion of the blades. This also indicates there is a negligible entrainment of ambient flow into the low-momentum wake. As a results of this isolation, the velocity deficit distribution is almost constant, both in shape and location of the minimum, along the streamwise direction as shown in Fig. 7a).

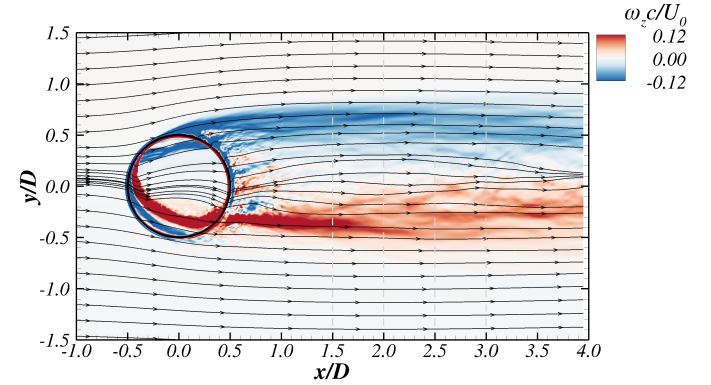


Fig. 6. Contours of normalised z-vorticity at $z/c = 1$ for the turbine rotating at $\lambda = 1.5$. Black circle represents the blades' swept perimeter.

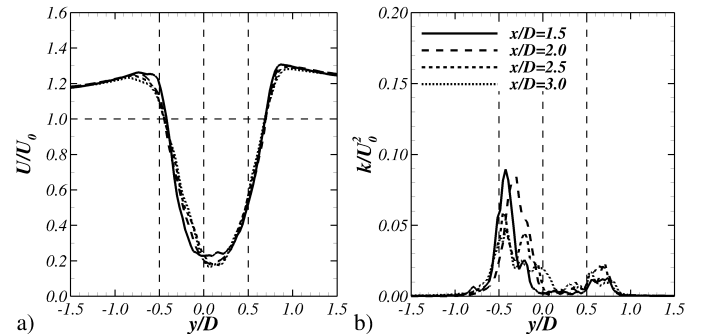


Fig. 7. Profiles of normalised mean streamwise velocity profiles and TKE at $x/D = 1.5, 2.0, 2.5,$ and 3.0 for the $\lambda = 1.5$ case. Black circle represents the blades' swept perimeter.

The wake uniformity found at $\lambda = 1.5$ is again represented by the location of the TKE peaks in the profiles of Fig. 7b). For $\lambda = 1.5$ these maxima are at $y/D \approx 0.4$ whereas for $\lambda = 2.0$ these are located at $y/D \approx 0.6$ indicating that there is a lower wake expansion for the lower rotational speed case. Noteworthy is that for $\lambda = 1.5$ the dynamic stall vortices are shed earlier during the upstroke rotation $0^\circ < \theta < 180^\circ$ than for the optimum tip speed ratio case [11]. The change in the blade-vortex interaction mechanics provokes that the TKE profiles do not show the two peaks found for $\lambda = 2.0$. At $\lambda = 1.5$ the vortices shed during the blades downstream

motion, i.e. $90^\circ < \theta < 270^\circ$, contain more energetic than those shed during the upstream motion of the blades, i.e. for $y/D > 0$.

Results for $\lambda=3.0$

At tip speed ratios above the optimum value, secondary effects dominate over those from dynamic stall [22]. Fig. 8 shows the contours of time-averaged spanwise vorticity with streamlines of the mean flow. The wake exhibits larger asymmetry than for $\lambda = 2.0$ (see Fig. 4), induced by the faster rotation of the blades, whilst its downstream extension shrinks. Such changes in the wake characteristics are due to the Magnus effect induced by the fast rotor rotation, which was previously identified and investigated in the flow around rotating cylinders [13].

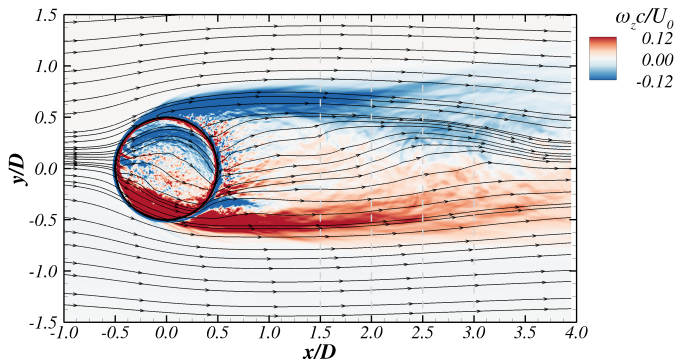


Fig. 8. Contours of normalised z-vorticity at $z/c = 1$ for the turbine operating at $\lambda = 3.0$.

The velocity profiles shown in Fig. 9a) evidence the rapid transition experienced in the wake in the $\lambda = 3.0$ case. Whilst the profile at $x/D = 1.5$ follows a similar distribution than that found for $\lambda = 2.0$, there is a faster velocity recovery in the wake at $x/D = 3.0$, as the minimum velocity value increases from approx. 0.2 to 0.6 between these locations. Additionally, the minimum velocity is clearly located in the $y/D > 0$ range at the profile closest to the turbine and there is a transition towards $y/D = 0$ observed at $x/D = 3.0$, which indicates the presence of the Magnus effect and how it enhances the wake velocity recovery.

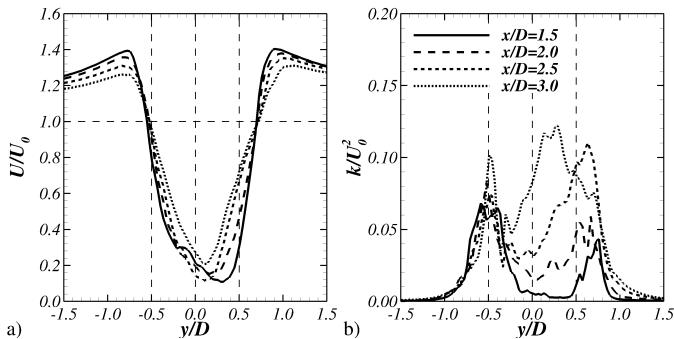


Fig. 9. Profiles of normalised mean streamwise velocity profiles and TKE at $x/D = 1.5, 2.0, 2.5$ and 3.0 for the $\lambda = 3.0$ case.

TKE profiles from Fig. 9b) depict another characteristic in the wake induced by the Magnus effect. The two-peak TKE distribution observed in the profiles from the cases of $\lambda = 1.5$ and 2.0 , is now only achieved at $x/D = 1.5$ and $x/D = 2.0$. Further downstream, the two high-vorticity streams converge towards the centre of the channel ($y/D = 0$) and trigger velocity fluctuations and thus TKE. Further investigation into the instantaneous motion of the wake at $\lambda = 3.0$ is required in order to identify the factors responsible for triggering TKE values downstream the device. Similar TKE transition is observed in the wake behind HATTs [11] where after tip vortices are diffused with the ambient flow, a low frequency wake meandering triggers TKE levels.

C. Centreline velocity distribution

Fig. 10 shows the normalised streamwise velocity values along the centreline of the domain, i.e. at $y/D = 0$, between $0 < x/D < 4$. The values of experiments and RANS correspond only to the optimum tip speed ratio whereas the present LES results are for tip speed ratios of $1.5, 2.0$ and 3.0 . For $\lambda = 2.0$, LES achieves a good agreement with both experiments and RANS with the region of minimum velocities located between $1.5 < x/D < 3$, and being the onset of wake recovery observed after $x/D \approx 3.5 - 4.0$. A similar velocity deficit distribution is obtained at $0.5 < x/D < 2.0$ regardless the rotational speed of the turbine. A faster wake recovery is observed for $\lambda = 3.0$ after $x/D = 3.0$ achieving a velocity of $U \approx 0.5U_0$ at $x/D = 4.0$ in contrast to the values of $U \approx 0.35U_0$ obtained in the lower rotational speed cases. The larger allowance of flow entrainment for $\lambda = 1.5$ is depicted from the relatively high velocity values at $0.5 < x/D$, i.e. within the inner wake.

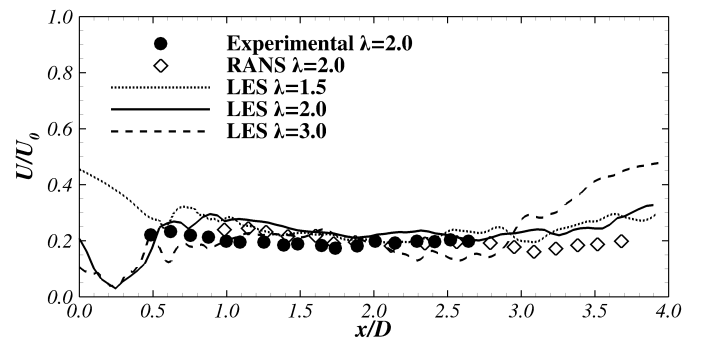


Fig. 10. Distribution of the normalised streamwise velocity along the centreline of the wake. Comparison of experimental and RANS values from [12] for the $\lambda = 2.0$ case, and present LES for $\lambda = 1.5, 2.0$ and 3.0 .

D. Parametrisation of the near-wake

Adopting cylinder-like representation of turbines can provide a rough estimation of the wake even though this approach might omit some of the main flow features [8], [9]. An obvious difference between a rotating VATT and a cylinder is that the former allows some flow to entrain through the rotor area, as observed in Fig. 10. It is possible to consider a

VATT as a porous cylinder whose porosity or entrainment rate is determined by its rotational speed and the geometric characteristics of the rotor. Following this argumentation, Araya et al. [9] introduced the dynamic solidity factor, σ_D defined in Eq. 7, and verified that it correlates well with the wake hydrodynamics, such as velocity deficit recovery and minimum velocity value.

$$\sigma_D = 1 - \frac{1}{2\pi\sigma\lambda} \quad (7)$$

According to Eq. 7, increasing either turbine solidity σ or tip speed ratio λ enlarges the dynamic solidity value. The latter enhances the blockage from the turbine in the approaching flow and thus it approaches the behaviour of a bluff body, i.e. $\sigma_D \approx 1.0$. Table I presents the values of σ_D for the different tip speed ratios adopted in the simulations.

TABLE I
DYNAMIC SOLIDITY VALUES FOR THE TIP SPEED RATIOS SIMULATED.

Tip speed ratio	1.5	2.0	2.5	3.0
Dynamic solidity	0.392	0.544	0.635	0.696

Araya et al. [9] found that for $\sigma_D > 0.65$ the velocity recovery rate increased. Only for the case of $\lambda = 3.0$ is above this threshold and interestingly is the case where the turbine wake is greatly influenced by the Magnus effect achieving a higher velocity deficit recovery as Fig. 10 illustrates. Although it is not possible to conclude that $\sigma_D > 0.65$ is the limit over which the Magnus effects magnifies and dominates the near-wake, the present results and those from [9] encourage to consider it as a representative limit.

V. CONCLUSION

The analysis of the near-wake developed downstream of a VATT operating at different rotational speeds has been presented. Velocity and turbulent kinetic energy results from the present large-eddy simulation approach are successfully validated with experimental data for the case the turbine rotated at its optimum tip speed ratio. The developed wake is laterally bounded by two high-vorticity streams of opposite sign as a result of the convection of the vortices shed from the blades during their rotation. The regions of highest turbulent kinetic energy are located along these streams which are well predicted by LES compared with the experimental observations. Results have also proved how the eddy-resolving nature of LES permits to perform a more accurate prediction of the turbulent quantities than RANS models, whose time-averaging nature damp the velocity fluctuations underestimating turbulent kinetic energy values. Nevertheless, both methods achieved a close match with experiments predicting the velocity deficit distribution.

The wake pattern changed considerably depending on the rotational speed of the turbine. The flow field developed at tip speed ratio of 3.0 reveal the domination of the Magnus effect in the enclosed wake which enhanced the velocity deficit

recovery. There was no evidence of the latter effect in the wake developed at tip speed ratio of 1.5 in which a greater amount of flow entrained the rotor swept area diminishing the blockage effect from the turbine.

Balancing flow entrainment through the rotor swept area as well as the Magnus effect is key in the prospective design of VATT arrays in order to optimise turbine-to-turbine interaction. Dynamic solidity accounts for the blockage generated by the rotating turbine at certain velocity and was used to parametrise the Magnus effect. A threshold of approx. 0.65 was found to be a good indicator above which the Magnus effect magnifies. Nonetheless, it does not consider the channel blockage which constrains the lateral expansion of the wake and thus changes wake properties when compared to open-channel flows. Further studies will focus on the differences in the wake developed in constrained and boundless channels and its relation to the Magnus effect. The present results encourage to study the combination of turbines with different solidities focused on their interaction as an alternative to increase the global power generation of the array.

ACKNOWLEDGEMENT

The authors thank the Engineering and Physical Science Research Council (EPSRC) for funding this research under the grant number EP/K502819/1. The simulations were performed using HPC Wales supercomputer facilities and this is herein acknowledged.

REFERENCES

- [1] European Commission, "Ocean Energy: Action needed to deliver on the potential of ocean energy by 2020 and beyond," Tech. Rep., 2014.
- [2] M. Khan, G. Bhuyan, M. Iqbal, and J. Quaicoe, "Hydrokinetic energy conversion systems and assessment of horizontal and vertical axis turbines for river and tidal applications: A technology status review," *Appl. Energy*, vol. 86, no. 10, pp. 1823–1835, 2009.
- [3] M. J. Churchfield, Y. Li, and P. J. Moriarty, "A large-eddy simulation study of wake propagation and power production in an array of tidal-current turbines," *Philos. Trans. A. Math. Phys. Eng. Sci.*, vol. 371, no. 1985, p. 20120421, 2013.
- [4] M. Kinzel, D. B. Araya, and J. O. Dabiri, "Turbulence in vertical axis wind turbine canopies," *Phys. Fluids*, vol. 27, no. 11, p. 115102, 2015.
- [5] S. Kang, X. L. Yang, and F. Sotiropoulos, "On the onset of wake meandering for an axial flow turbine in a turbulent open channel flow," *J. Fluid Mech.*, vol. 744, pp. 376–403, 2014.
- [6] P. Ouro, M. Harrold, T. Stoesser, and P. Bromley, "Hydrodynamic loadings on a horizontal axis tidal turbine prototype," *J. Fluids Struct.*, vol. 71, pp. 78–95, 2017.
- [7] G. Tescione, D. Ragni, C. He, C. J. Simão Ferreira, and G. J. W. van Bussel, "Near wake flow analysis of a vertical axis wind turbine by stereoscopic particle image velocimetry," *Renew. Energy*, vol. 70, pp. 47–61, 2014.
- [8] P. Bachant and M. Wosnik, "Characterising the near-wake of a cross-flow turbine," *J. Turbul.*, vol. 16, no. 4, pp. 392–410, apr 2015.
- [9] D. B. Araya, T. Colonius, and J. O. Dabiri, "Transition to bluff-body dynamics in the wake of vertical-axis wind turbines," *J. Fluid Mech.*, vol. 813, pp. 346–381, 2017.
- [10] S. Shamsoddin and F. Porté-Agel, "Large eddy simulation of vertical axis wind turbine wakes," *Energies*, vol. 7, no. 2, pp. 890–912, 2014.
- [11] P. Ouro and T. Stoesser, "An immersed boundary-based large-eddy simulation approach to predict the performance of vertical axis tidal turbines," *Comput. Fluids*, vol. 152, pp. 74–87, 2017.
- [12] G. Mercier, C. Pellone, and T. Maitre, "Experimental characterization of the near-wake of a cross flow water turbine with LDV measurements," in *17th Int. Symp. Appl. Laser Tech. to Fluid Mech.*, 2014, pp. 1–8.

- [13] S. J. Karabelas, "Large Eddy Simulation of high-Reynolds number flow past a rotating cylinder," *Int. J. Heat Fluid Flow*, vol. 31, no. 4, pp. 518–527, 2010.
- [14] T. Stoesser and V. I. Nikora, "Flow structure over square bars at intermediate submergence: Large Eddy Simulation study of bar spacing effect," *Acta Geophys.*, vol. 56, no. 3, pp. 876–893, 2008.
- [15] B. Fraga, T. Stoesser, C. C. Lai, and S. A. Socolofsky, "A LES-based EulerianLagrangian approach to predict the dynamics of bubble plumes," *Ocean Model.*, vol. 97, pp. 27–36, jan 2016.
- [16] A. J. Chorin, "Numerical solution of the Navier-Stokes equations," *Math. Comput.*, vol. 22, no. 104, pp. 745–762, 1968.
- [17] A. Cristallo and R. Verzicco, "Combined Immersed Boundary/Large-Eddy-Simulations of Incompressible Three Dimensional Complex Flows," *Flow, Turbul. Combust.*, vol. 77, pp. 3–26, 2006.
- [18] F. Nicoud and F. Ducros, "Subgrid-scale stress modelling based on the square of the velocity gradient tensor," *Flow, Turbul. Combust.*, vol. 62, no. 3, pp. 183–200, 1999.
- [19] M. Uhlmann, "An immersed boundary method with direct forcing for the simulation of particulate flows," *J. Comput. Phys.*, vol. 209, no. 2, pp. 448–476, 2005.
- [20] A. M. Roma, C. S. Peskin, and M. J. Berger, "An adaptive version of the immersed boundary method," *J. Comput. Phys.*, vol. 153, no. 2, pp. 509–534, 1999.
- [21] D. B. Araya and J. O. Dabiri, "A comparison of wake measurements in motor-driven and flow-driven turbine experiments," *Exp. Fluids*, vol. 56, p. 150, 2015.
- [22] T. Maître, E. Amet, and C. Pellone, "Modeling of the flow in a Darrieus water turbine: Wall grid refinement analysis and comparison with experiments," *Renew. Energy*, vol. 51, pp. 497–512, 2013.